Electronic Supplementary Material (ESI) for Green Chemistry.
This journal is © The Royal Society of Chemistry 2023

Supporting Information

Red, Yellow, Green, and Blue Light-Emitting High-Crystallized Graphene Quantum Dots Derived from Lignin: Controllable Syntheses and Light-Emitting Diode Applications

Tian Gao,*[a] Shengnan Guo,[a] Jiaojiao Zhang,[a] Jintao Chen,[a] Shiru Yin,[a] Na Peng,[a] Qun Cai,[a] Huan Xu,[a] and Yi Liu*[a,b]

a School of Chemistry and Chemical Engineering, Hubei Province Key Laboratory for Coal Conversion and New Carbon Materials, Institute of Advanced Materials and Nanotechnology, Wuhan University of Science and Technology, Wuhan, 430081 P. R. China

b School of Chemical and Environmental Engineering, Wuhan Polytechnic University, Wuhan, 430023, P. R. China

Corresponding Author: Yi Liu and Tian Gao

E-mail: yiliuchem@whu.edu.cn
gaotian@whu.edu.cn

Table of Contents

Supporting information 19: Comparison of FT-IR spectra of lignin and four GQDs in the range of 1100- 1800 cm^{-1}.

Supporting information 20: Comparison of peak transmittance of FT-IR spectra of B-GQDs and their raw materials.

Supporting information 22: Comparison of peak transmittance of FT-IR spectra of Y-GQDs and their raw materials.

Supporting information 23: Comparison of peak transmittance of FT-IR spectra of R-GQDs and their raw materials.

Supporting information 24: Comparison of peaks of FT-IR spectra of the four GQDs.

Supporting information 25: The Raman spectra and XRD patterns of the four GQDs.

Supporting information 26: The atomic percentages of various elements in the four GQDs and their corresponding quantum yields.

Supporting information 27: Proportions of each chemical bond in the XPS fine spectra of the four GQDs.

Supporting information 28: Compare the ratio of sp^2 C to sp^3 C in the four GQDs.

Supporting information 29: ^{1}H NMR of GQDs during hydrothermal reaction.

Supporting information 30: Illuminance diagram of individual UV chip.

Supporting information 31: Stability demonstration of multi-colour LEDs.

Supporting information 32: Illumination of the UV lamp chip and four LEDs, along with the assessment of LED conversion efficiency.

Supporting information 1: Summary of the latest research progress in the preparation of carbon nanodots from lignin (2016-2023), comparing the properties and applications of different carbon dots synthesized by different technologies.

Table S1. Different processes of lignin-based carbon dots preparation during 2016-2023.

C-dots	Reference	Dopant atoms	Synthesis Method	Reagent	Crystallinity	Height (nm)	Year
CDs	1	/	Hydrothermal	H_2O_2	Medium	/	2016
r-FCDs	2	/	Microwave Irradiation	$NaBH_4$	Low	/	2017
GQDs	3	N	Hydrothermal	HNO_3	Medium	2	2018
LGQDs	4	N, S	Hydrothermal	O-aminobenzenesulfonic Acid, P-toluenesulfonic acid, Benzenesulfonic acid, Citric acid	Medium	1.7	2019
Mn-LGQD	5	Mn	Hydrothermal	HNO_3	Medium	1	2020
CDs	6	N, S	Hydrothermal	L-cysteine	Low	/	2021
B-GQDs, G-GQDs	7	N, S	Hydrothermal	Mild Organic acid	Medium	/	2022
NL-CDs	8	/	Microwave-assisted	/	Medium	/	2023

B-GQDs	/	N	Hydrothermal	/	**High**	**< 1**	**This work**
G-GQDs		N		Arginine			
Y-GQDs		/		NaOH			
R-GQDs		N, P					

Table S2. Comparison of luminescence properties of lignin-based carbon dots synthesized from 2016 to 2023.

C-dots	Reference	Emission Wavelength (nm)	Wavelength width (nm)	Colour	Application	Year	QY (%)
CDs	1	430	/	Blue	Cell Imaging	2016	/
r-FCDs	2	475	/	Blue	Nano-Drug Carrier and Bioimaging	2017	47.3
GQDs	3	410	/	Blue	Multicoloured Bioimaging	2018	21
LGQDs	4	488	/	Blue	Biosensor	2019	21
Mn-LGQD	5	420	/	Blue	Ion detection	2020	23, 31.6
CDs	6	450	/	Blue	battery	2021	/
B-GQDs, G-GQDs	7	475, 400	75	Blue, Green	/	2022	5.2, 23.7
NL-CDs	8	462	/	Blue	encryption	2023	5.97, 30.6
B-GQDs, G-GQDs, Y-GQDs, R-GQDs	/	**440, 520, 580, 625**	**185**	Blue, Green, Yellow, Red	**LEDs**	**This work**	**1.51, 0.86, 1.15, 4.66**

Supporting information 2: Excitation-emission spectral values and redshifts of the four GQDs.

Table S3. Excitation-emission spectral expressions and redshifts of the four GQDs.

Sample	$\lambda_{ex\ start}$ (nm)	$\lambda_{em\ start}$ (nm)	$\lambda_{ex\ end}$ (nm)	$\lambda_{em\ end}$ (nm)	Redshift (nm)
B-GQDs	310	442	550	622	180
G-GQDs	380	507	560	623	117
Y-GQDs	380	549	560	586	37
R-GQDs	410	540	590	630	90

Supporting information 3: Maximum excitation-emission spectra, half bandwidth and optimal emission wavelength at 370 nm excitation for the four GQDs.

Table S4. The maximum excitation-emission wavelengths, half-peak widths and optimal emission wavelengths at 370 nm excitation correspond to the four GQDs.

Sample	$\lambda_{ex\ max}$ (nm)	$\lambda_{em\ max}$ (nm)	FHWM (nm)	λ_{ex}=370 nm
B-GQDs	370	444	93	444
G-GQDs	460	553	158	489
Y-GQDs	520	580	107	535
R-GQDs	510	628	150	510

Supporting information 4: Emission spectra and CIE coordinates of Y-GQDs under 375 nm excitation in seven organic solvents.

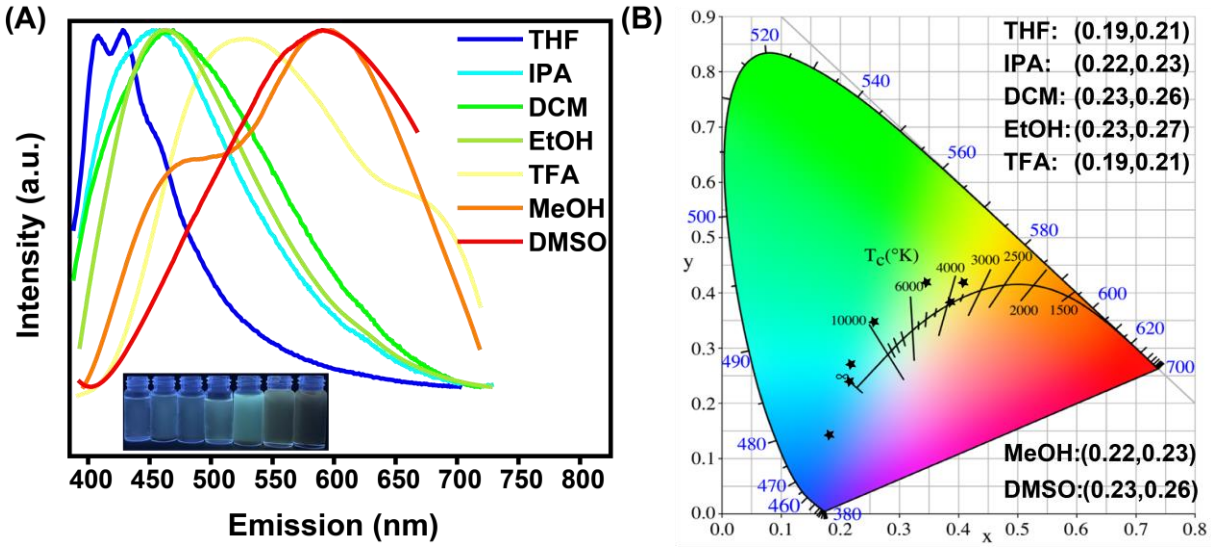

Figure S1. Normalized emission spectra (A) and CIE coordinates (B) of Y-GQDs under 375 nm excitation in seven organic solvents.

3 ml tetrahydrofuran, isopropyl alcohol, dichloromethane, ethanol, trifluoroacetic acid, methanol, and dimethyl sulfoxide were added to GQDs and were fully dissolved by ultrasound for 10 min.

Supporting information 5: Normalized optimal emission spectra and CIE coordinates of the four GQDs in the aqueous phase.

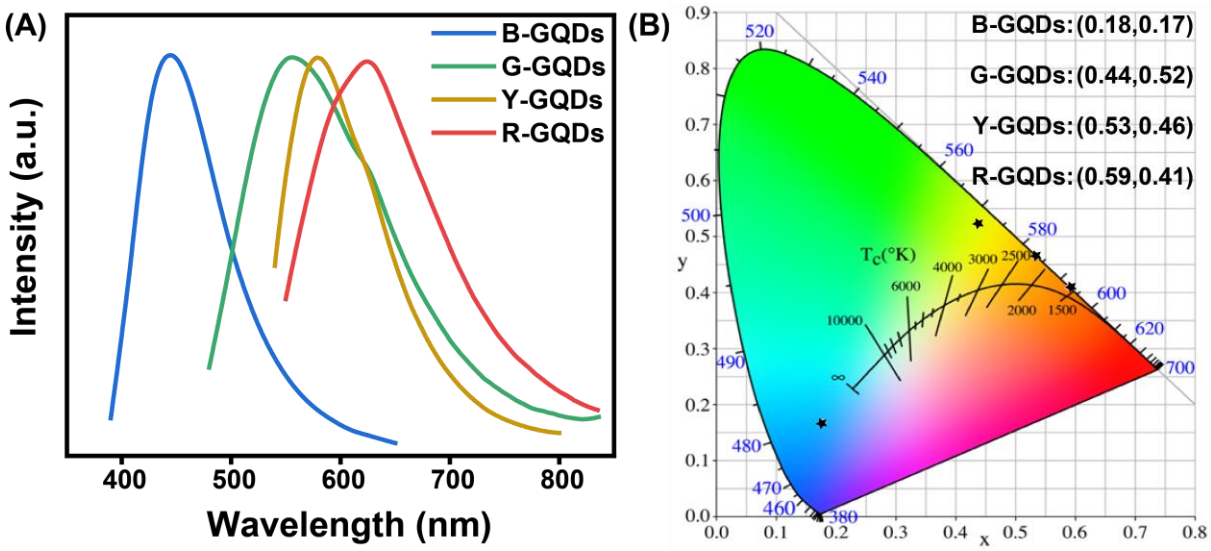

Figure S2. Normalized maximum intensity emission spectrum(A) and CIE coordinates of the four GQDs (B) in the aqueous phase.

Supporting information 6: Normalized optimal emission spectra and CIE coordinates of the four GQDs in the ethanol phase.

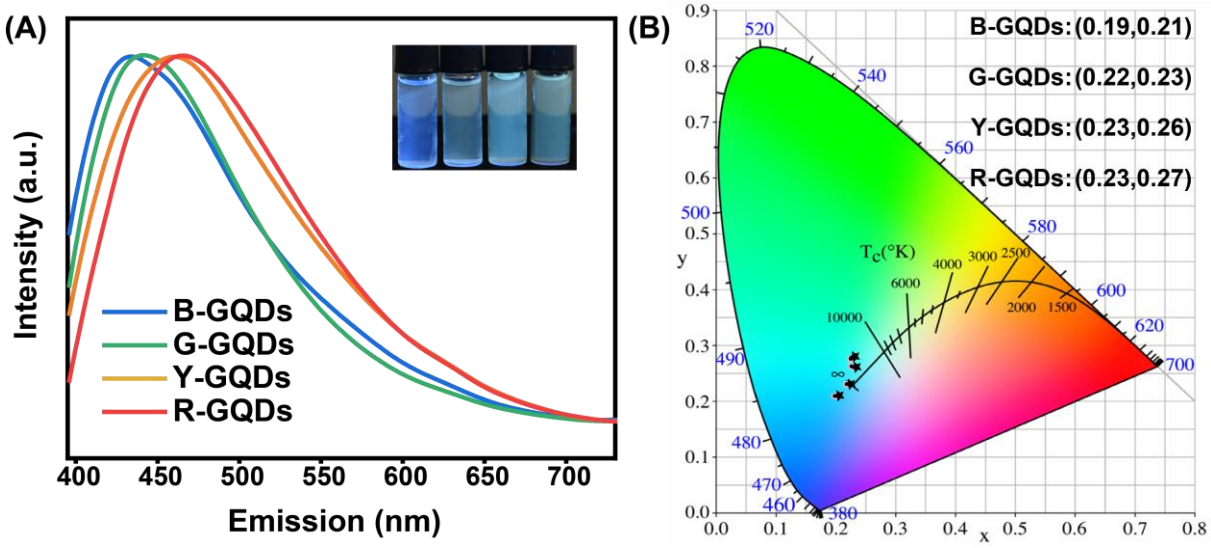

Figure S3. Normalized emission spectra (A) and CIE Coordinates (B) of the four GQDS excited at 375nm in the ethanol phase.

Supporting information 7: Fluorescence decay spectra of the four GQDs in the aqueous phase.

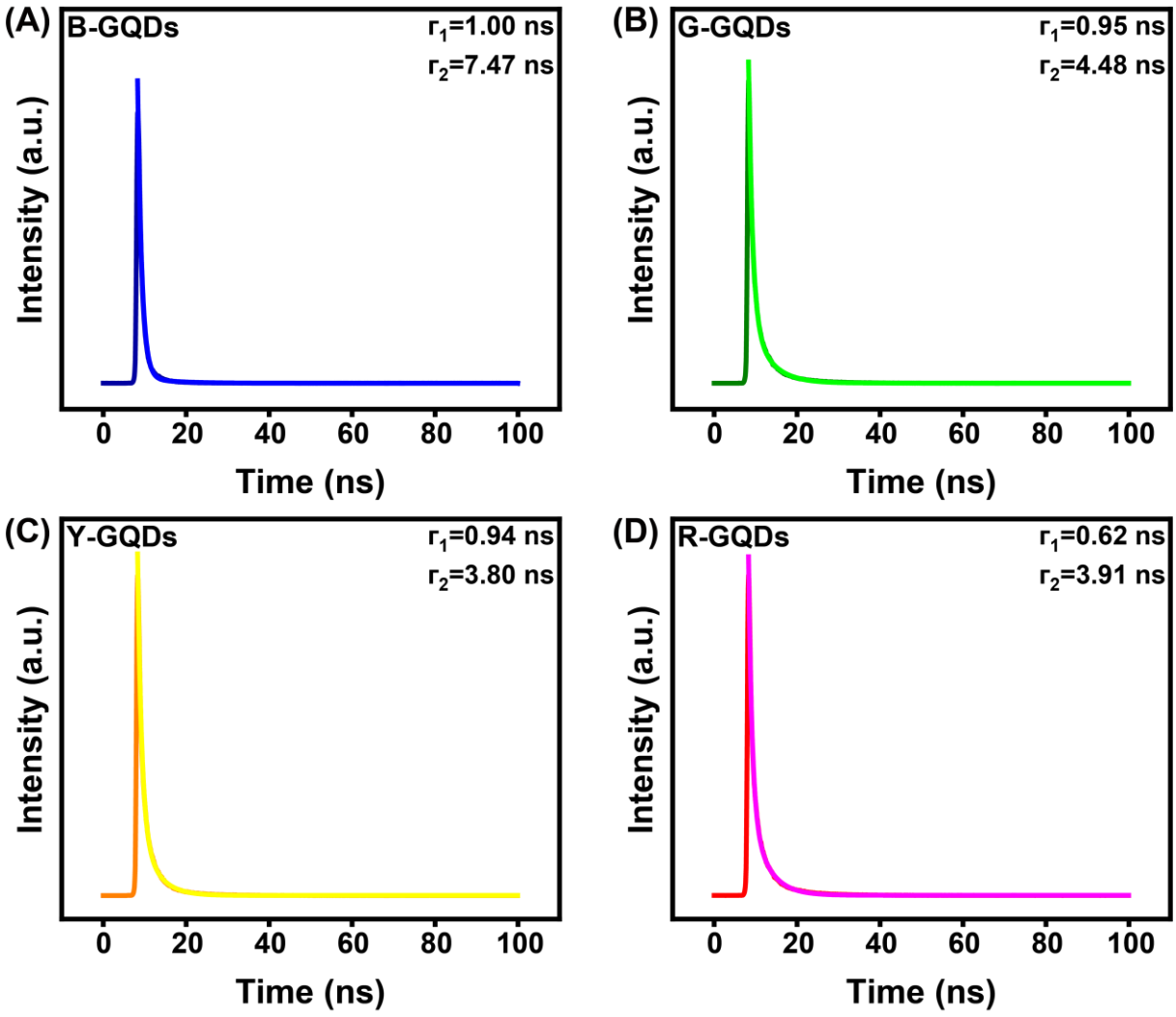

Figure S4. Time-resolved PL decay curves of aqueous solutions of four GQDs at 375 nm excitation.

Supporting information 8: Comparison of the fluorescence lifetimes of the four GQDs dispersions in the aqueous phase.

Table S5. FL attenuation curve fitting parameters of the four GQDs dispersions in the aqueous phase.

Sample	τ_1 (ns)	B_1(%)	τ_2 (ns)	B_2(%)	τ_{avg} (ns)	R^2
B-GQDs	1.00	98.27	7.47	1.73	1.12	0.995
G-GQD	0.95	80.64	4.48	19.36	1.63	0.998
Y-GQD	0.94	79.12	3.80	20.88	1.54	0.998
R-GQD	0.83	76.30	3.96	23.70	1.57	0.998

Supporting information 9：Absolute quantum yield of the four GQDs in the ethanol phase.

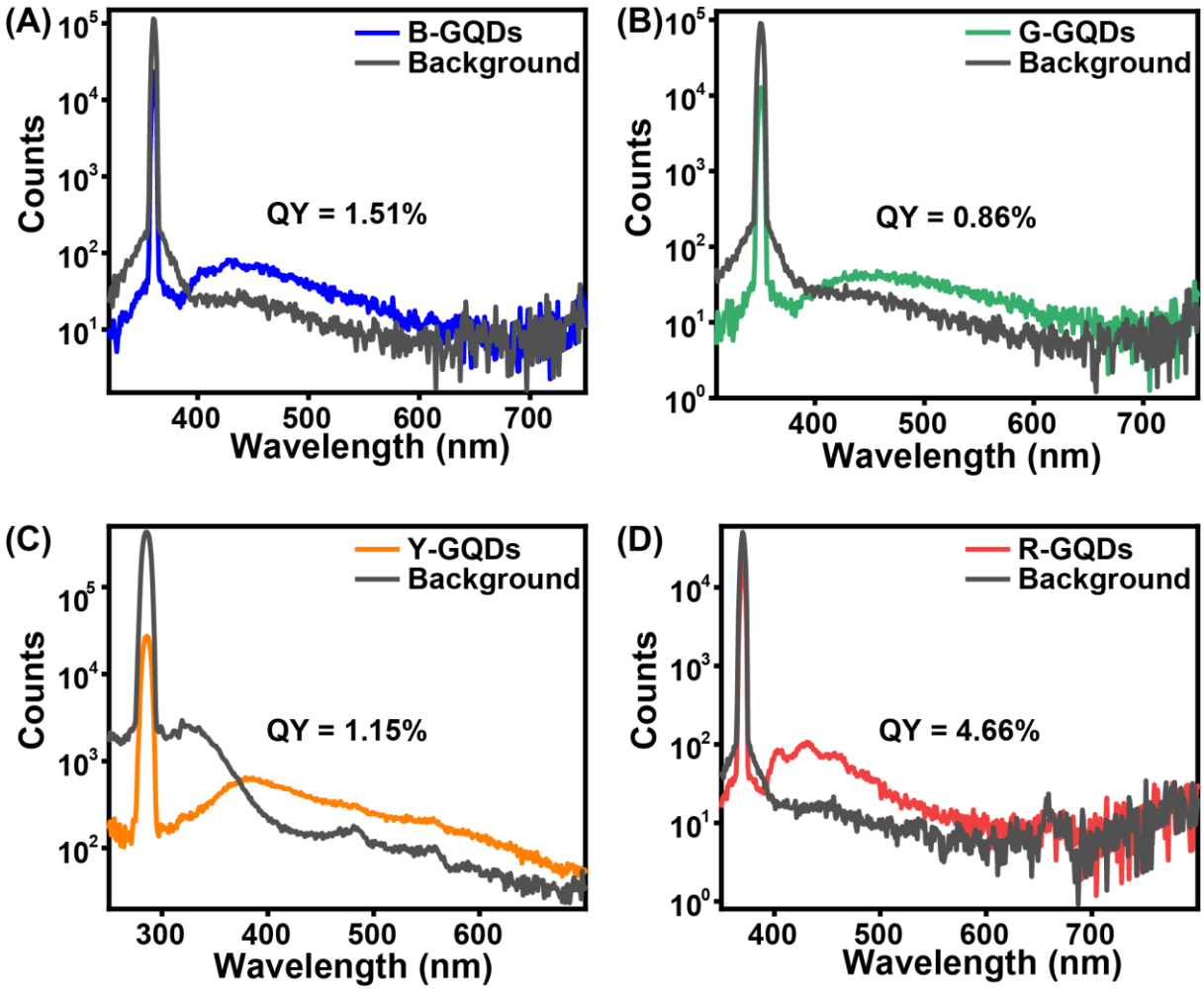

Figure S5. The absolute quantum yield of B-, G-, Y-, R- GQDs in ethanol phase.

Supporting information 10: The band gaps of the four GQDs were calculated from their absorption spectra.

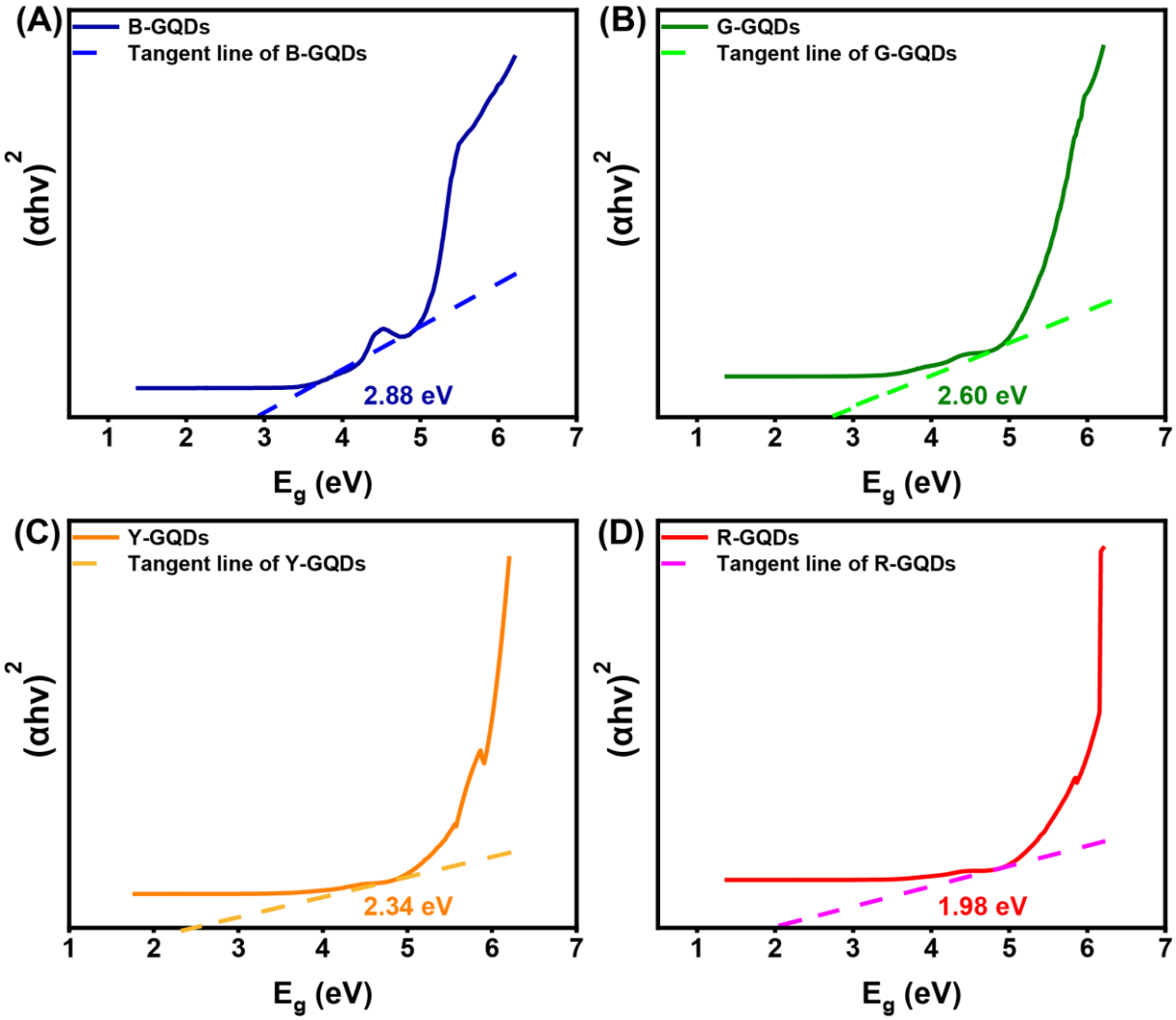

Figure S6. The band gap of B-, G-, Y-, R- GQDs were calculated from their absorption margin.

To confirm the changes in band gap of the four GQDs, UV-vis absorption data were utilized to calculate their optical band gap values using the Tauc relationship (**Figure S6**). The Tauc relationship [9] used in the calculation of the optical band gap is given by the formula

$$(\alpha h\nu)^{n} = A\,(h\nu - E_g)$$

where α is the absorption coefficient, hv is the photon energy, A is a constant, E_g is the optical band gap, and n is an empirical constant. The absorption value Abs, which is proportional to the absorption coefficient α, is used as the ordinate in the obtained spectrum. Whether Abs or α is employed in the Tauc plot to calculate E_g, the value of E_g remains unaffected. In this study, assuming GQDs as a direct band gap material, the value of n = 1/2 was utilized. Figure S6

illustrates the plot of $(\alpha hv)^2$ versus hv for the four GQDs. The optical band gap (E_g) is determined by linear fits of the $(\alpha hv)^2$ and hv curves, considering the intercept of the energy (*hv*) axis. The estimated optical band gaps from these fits are 2.88 eV, 2.60 eV, 2.34 eV, and 1.98 eV for B-GQDs, G-GQDs, Y-GQDs, and R-GQDs, respectively. These values are consistent with the equation $E_g = 1240/\lambda_g$, which is used to calculate the energy band gap from the emission wavelength. Based on our results, it is confirmed that the increasing size of R-GQDs and the introduction of heteroatoms contribute to a lower band gap compared to B-GQDs.

Supporting information 11: Fluorescence emission spectra of GQDs and CDs.

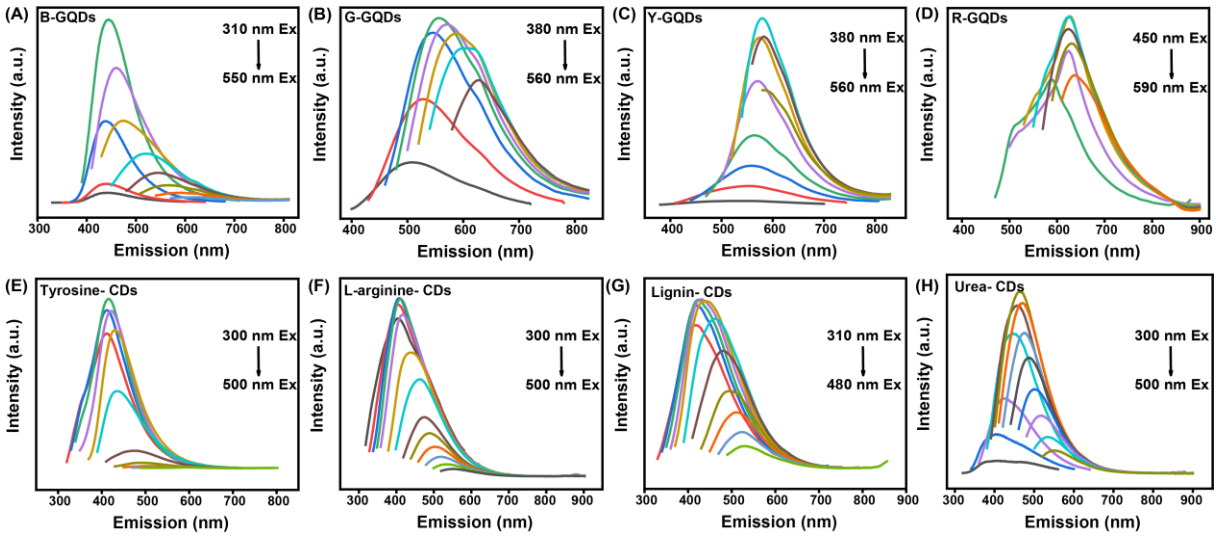

Figure S7. Comparison of fluorescence emission spectra of GQDs and CDs prepared by a single precursor system.

Supporting information 12: Comparison of the PL properties of GQDs and CDs.

Table S6. Comparison of the PL properties of GQDs and CDs prepared from a single precursor.

Sample	Emission peak (nm)	Sample	Emission peak (nm)
B-GQDs	444	Tyrosine- CDs	415
G- GQDs	553	L-arginine- CDs	408
Y- GQDs	580	Lignin- CDs	429
R- GQDs	628	Urea- CDs	463

Supporting information 13: The yields of GQDs and CDs.

Table S7. The yields of prepared GQDs and CDs.

Sample	Productivity (%)	Sample	Productivity (%)
B-GQDs	10.2	Tyrosine- CDs	4.3
G- GQDs	16.5	L-arginine- CDs	2.3
Y- GQDs	54.7	Lignin- CDs	3.4
R- GQDs	46.3	Urea- CDs	7.5

Supporting information 14: The variation in photoluminescence (PL) intensity with excitation time was investigated for GQDs using a 365 nm UV lamp (8W).

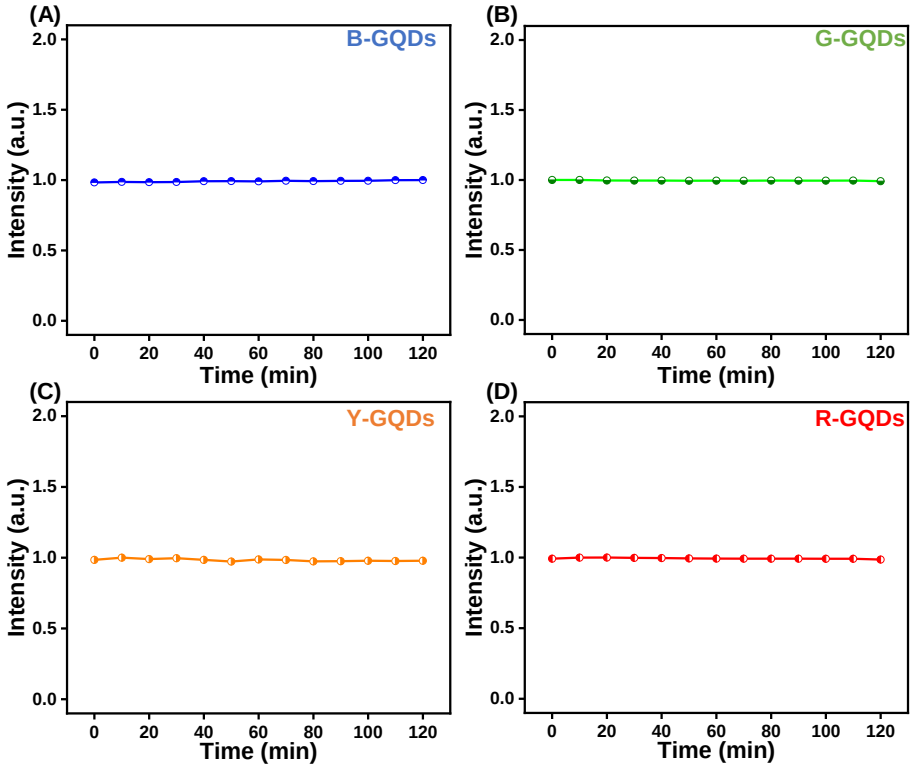

Figure S8. Dependence of PL intensity on excitation time for GQDs under 365 nm UV Lamp(8W).

Supporting information 15: The relationship between PL intensity and excitation time was examined at the maximum excitation wavelength forGQDs.

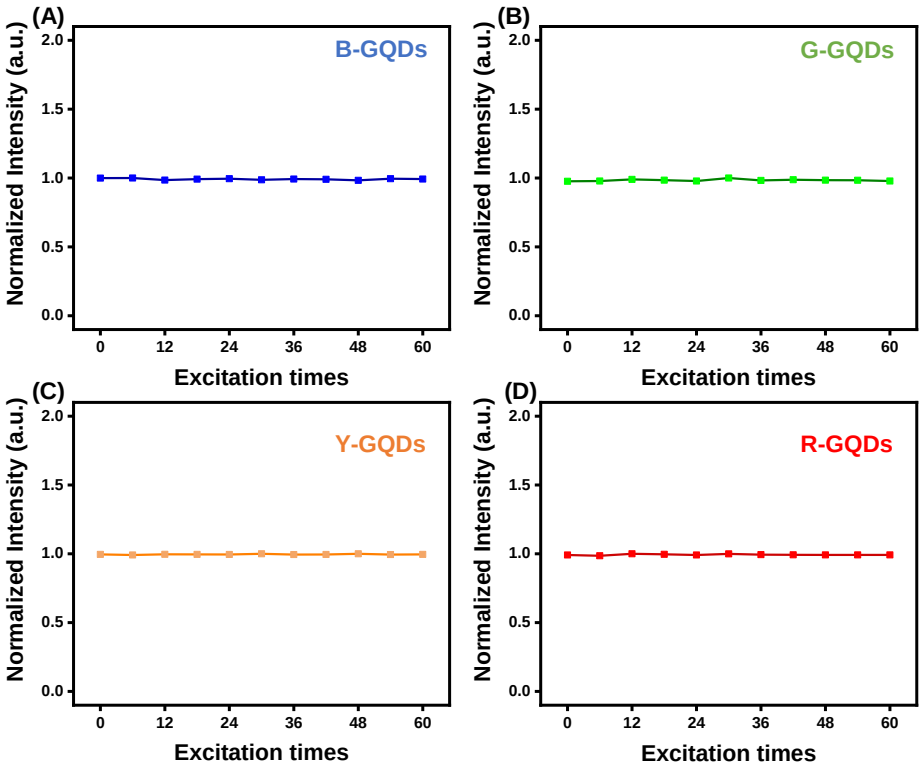

Figure S9. Dependence of PL intensity on excitation times at maximum excitation wavelength for GQDs.

Supporting information 16: The impact of ionic strength on the photoluminescence (PL) intensity of GQDs was assessed by manipulating ionic strength through different concentrations of NaCl.

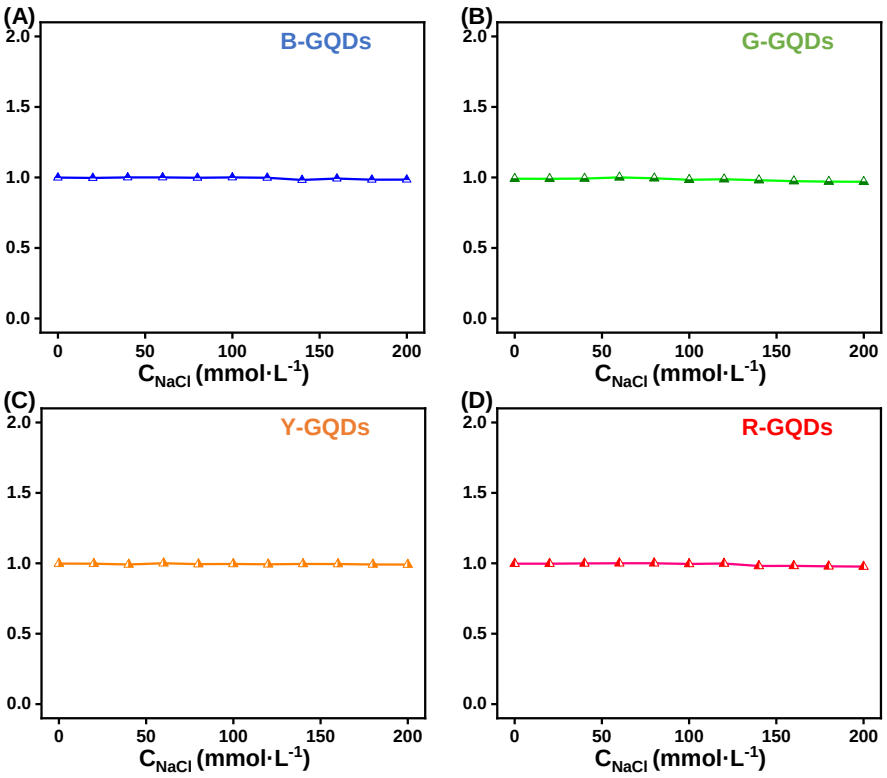

Figure S10. Effect of ionic strengths on the PL intensity of GQDs (ionic strengths were controlled by various concentrations of NaCl.

Supporting information 17: Hydration particle size and ζ potential of the four GQDs in the aqueous phase.

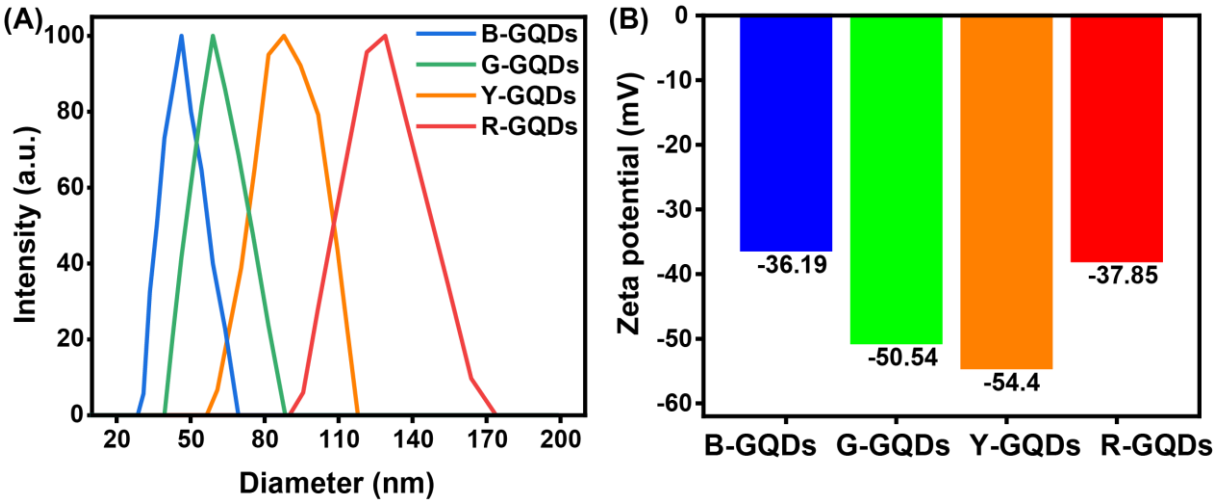

Figure S11. Hydration particle size (A) and ζ potential (B) of B-, G-, Y-, R- GQDs in the aqueous phase.

Supporting information 18: Fourier infrared spectra of the four GQDs and their corresponding raw materials.

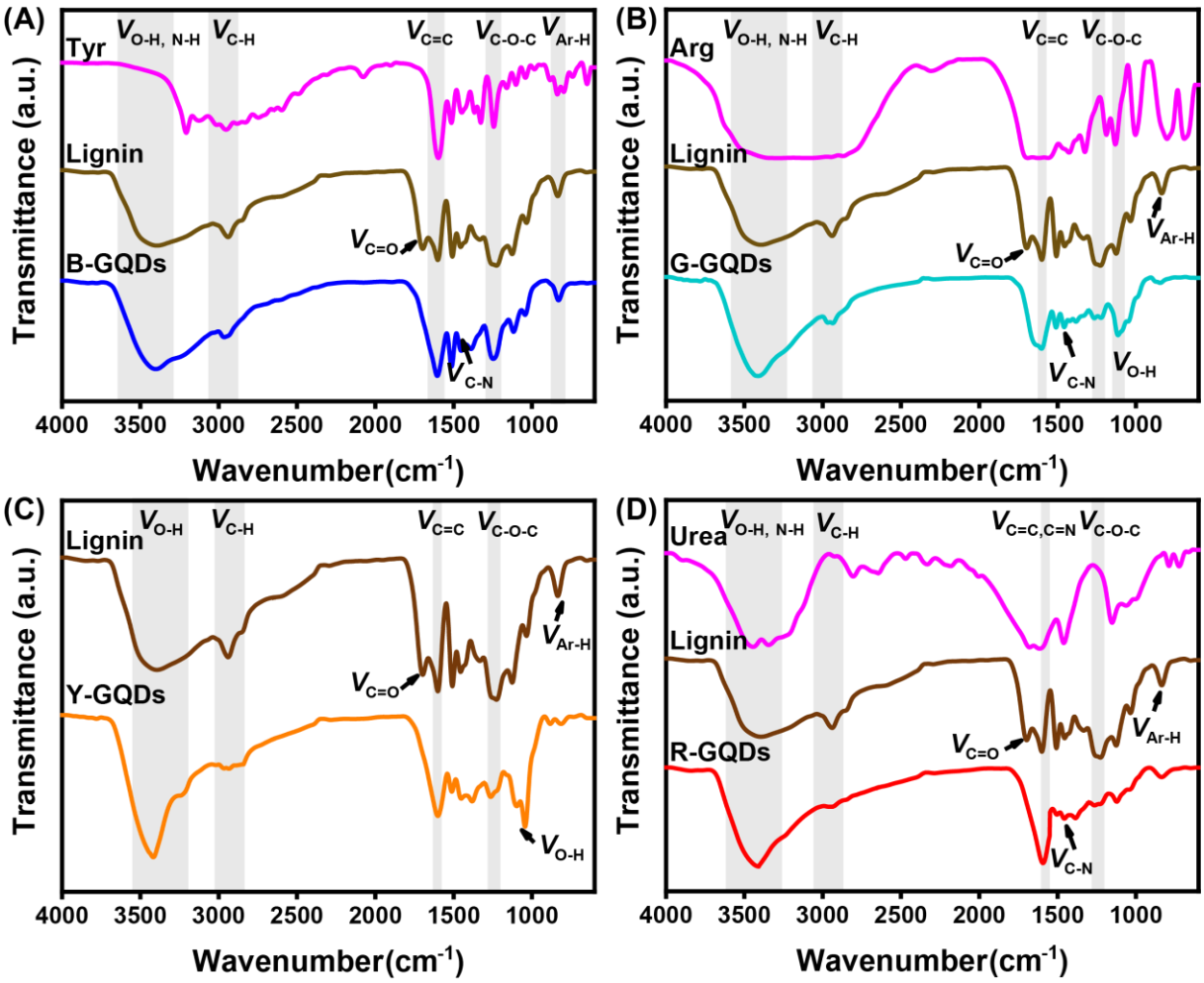

Figure S12. Comparison of FT-IR spectra of the four GQDs with their corresponding raw materials.

Supporting information 19: Comparison of FT-IR spectra of lignin and four GQDs in the range of 1100- 1800 cm^{-1}.

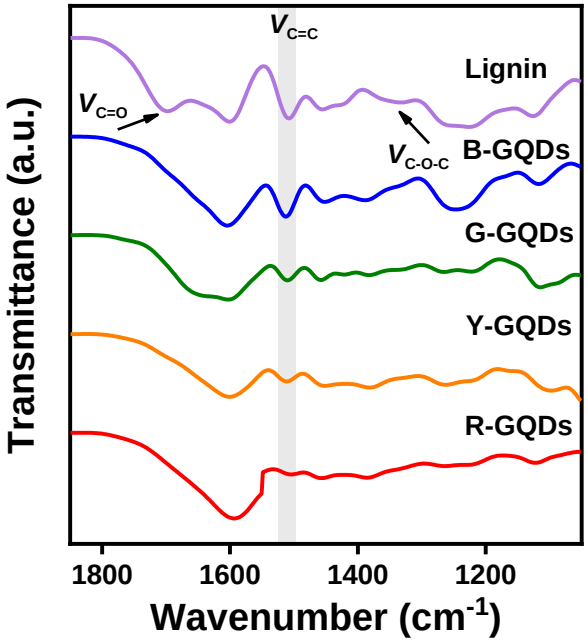

Figure S13. FT-IR spectra of lignin and four GQDs in the range of 1100- 1800 cm^{-1}.

Supporting information 20: Comparison of peak transmittance of FT-IR spectra of B-GQDs and their raw materials.

Table S8. Comparison of transmittance peaks of tyrosine, lignin, and B-GQDs by FT-IR spectra.

Sample (Position / cm^{-1})	O-H/N-H (3405)	C-H (2941)	C=O (1695)	C=C (1600)	C-N (1452)	C-O (1244)	Ar-H (835)
Tyrosine	0.90	0.30	0.89	0.003	0.48	0.33	0.67
Lignin	0.22	0.30	0.18	0.06	/	0.01	0.73
B-GQDs	0.08	0.80	0. 57	0.004	0.26	0.18	0.80

Supporting information 21: Comparison of peak transmittance of FT-IR spectra of G-GQDs and their raw materials.

Table S9. Comparison of absorption peaks of arginine, lignin, and G-GQDs by FT-IR spectra.

Sample (Position / cm^{-1})	$\nu_{O-H/N-H}$ (3419)	C-H (2928)	C=O (1695)	C=C (1600)	C-N (1452)	C-O (1244)	δ_{O-H} (1117)	Ar-H (846)
Arginine	0.03	0.02	0.001	0.003	0.09	0.58	0.24	0.37
Lignin	0.22	0.32	0.18	0.06	/	0.01	0.15	0.76
G-GQDs	0.00	0.54	0. 63	0.27	0.50	0.60	0.41	0.94

Supporting information 22: Comparison of peak transmittance of FT-IR spectra of Y-GQDs and their raw materials.

Table S10. Comparison of absorption peaks between lignin and Y-GQDs by FT-IR spectroscopy.

Sample	O-H	C-H	C=O	C=C	C-O-C	O-H	Ar-H
(Position / cm^{-1})	(3419)	(2940)	(1695)	(1600)	(1244)	(1047)	(837)
Lignin	0.22	0.32	0.18	0.06	0.01	0.15	0.76
Y-GQDs	0.00	0.62	0. 72	0.29	0.45	0.22	0.96

Supporting information 23: Comparison of peak transmittance of FT-IR spectra of R-GQDs and their raw materials.

Table S11. Comparison of absorption peaks of urea, lignin, and R-GQDs by FT-IR spectra.

Sample	O-H/N-H	C-H	C=O	C=C	C-N	C-O	Ar-H
(Position / cm^{-1})	(3419)	(2928)	(1695)	(1600)	(1452)	(1244)	(846)
Urea	0.04	0.93	0.03	0.01	0.07	0.81	0.93
Lignin	0.22	0.32	0.18	0.06	/	0.01	0.76
R-GQDs	0.004	0.60	0. 63	0.29	0.49	0.63	0.91

Supporting information 24: Comparison of peaks of FT-IR spectra of the four GQDs.

Table S12. Comparison of FT-IR spectral peaks of the four GQDs.

Sample	O-H/ N-H	C-H	C=O	C=C	C-N	C-O	O-H	Ar-H
(Position / cm^{-1})	(3419)	(2928)	(1695)	(1600)	(1452)	(1244)	(1117)	(846)
B-GQDs	0.08	0.80	0. 57	0.004	0.26	0.18	0.84	0.80
G-GQDs	0.00	0.54	0. 63	0.27	0.50	0.60	0.41	0.94
Y-GQDs	0.00	0.62	0. 72	0.29	/	0.45	0.40	0.96
R-GQDs	0.004	0.60	0. 63	0.29	0.49	0.63	0.66	0.91

Supporting information 25: The Raman spectra and XRD patterns of the four GQDs.

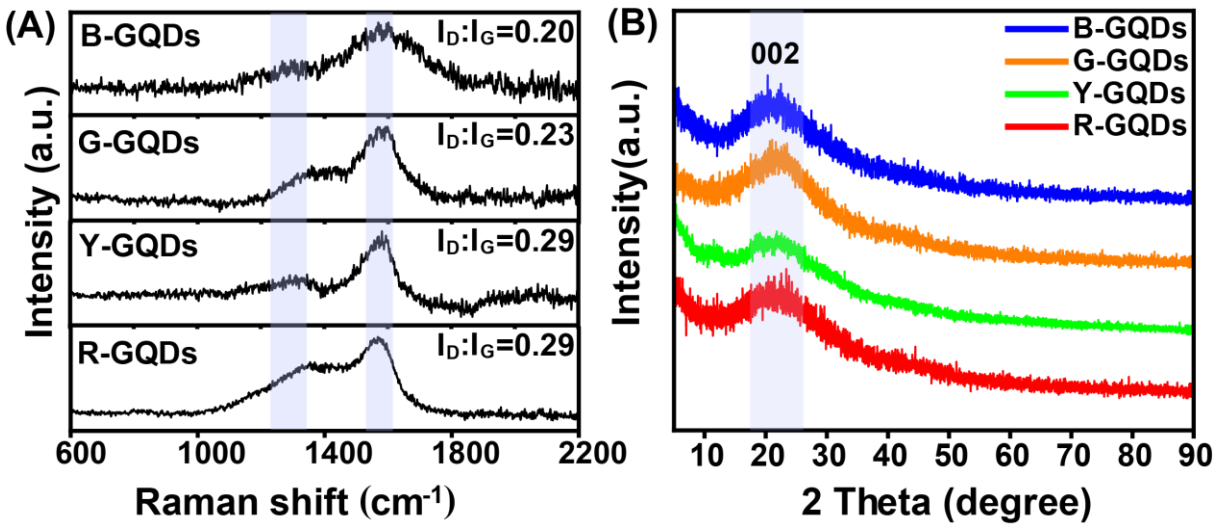

Figure S14. The Raman spectra (A) and XRD patterns (B) of R-GQDs, Y- GQDs, G- GQDs and B-GQDs, respectively.

Supporting information 26: The atomic percentages of various elements in the four GQDs and their corresponding quantum yields.

Table S13. Atomic percentages of various factors and their ratios in the four GQDs.

Sample	C 1s (%)	O 1s (%)	N 1s (%)	P 2p (%)	C/O	C/N	QY (%)
B-GQDs	72.10	23.77	4.13	/	3.03	17.46	1.51
G-GQD	69.12	24.92	5.96	/	2.77	11.60	0.86
Y-GQD	71.19	28.81	/	/	2.47	/	1.15
R-GQD	66.91	29.71	2.41	0.97	2.25	27.76	4.66

Supporting information 27: Proportions of each chemical bond in the XPS fine spectra of the four GQDs.

Table S14. The relative concentration of diverse function groups in the four GQDs according to HRXPS analytic judgment.

Sample	C 1s			O 1s		
	C-C/C=C (%)	C-N/C-O (%)	O-C=O (%)	C=O (%)	C-O/O-H (%)	O-C=O (%)
peak position (eV)	284.8	286.2	288.0	531.2	532.1	533.2
B-GQDs	61.70	28.99	9.31	21.20	52.16	26.64
G-GQD	63.25	31.01	5.74	29.46	43.46	27.08
Y-GQD	62.43	27.00	10.57	17.31	47.05	35.64
R-GQD	62.91	21.55	15.54	24.61	39.09	36.30

Sample	N 1s		
	C-N (%)	N-H (%)	Graphitic-N (%)
peak position (eV)	399.1	400.0	401.0
B-GQDs	40.55	40.63	18.82
G-GQD	20.81	51.75	27.44
Y-GQD	/	/	/
R-GQD	24.63	44.60	30.77

Supporting information 28: Compare the ratio of sp^2 C to sp^3 C in the four GQDs.

Table S15. Proportions of sp^2 C and sp^3 C in the four GQDs.

Sample	sp^2 C	sp^3 C	sp^2 C/ sp^3 C
	C-C/C=C (%)	C-N/C-O (%)	
B-GQDs	61.70	28.99	2.12
G-GQD	63.25	31.01	2.04
Y-GQD	62.43	27.00	2.31
R-GQD	62.90	21.55	2.92

Supporting information 29: ^{1}H NMR of GQDs during hydrothermal reaction.

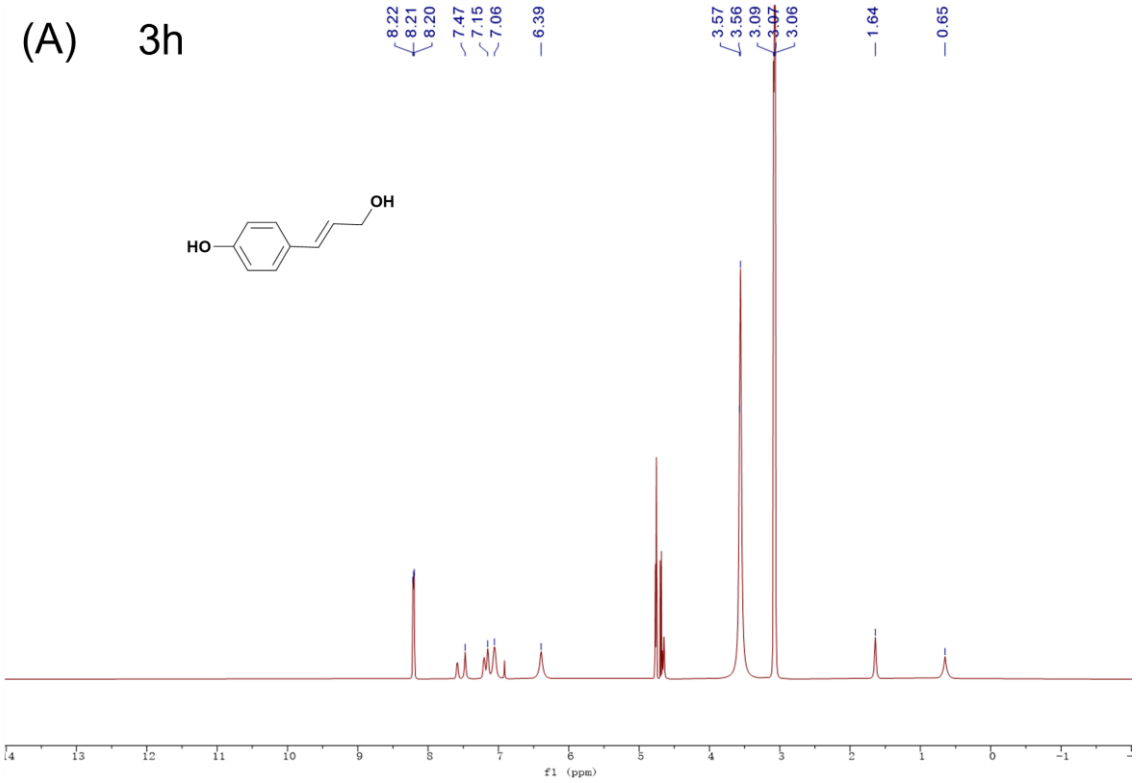

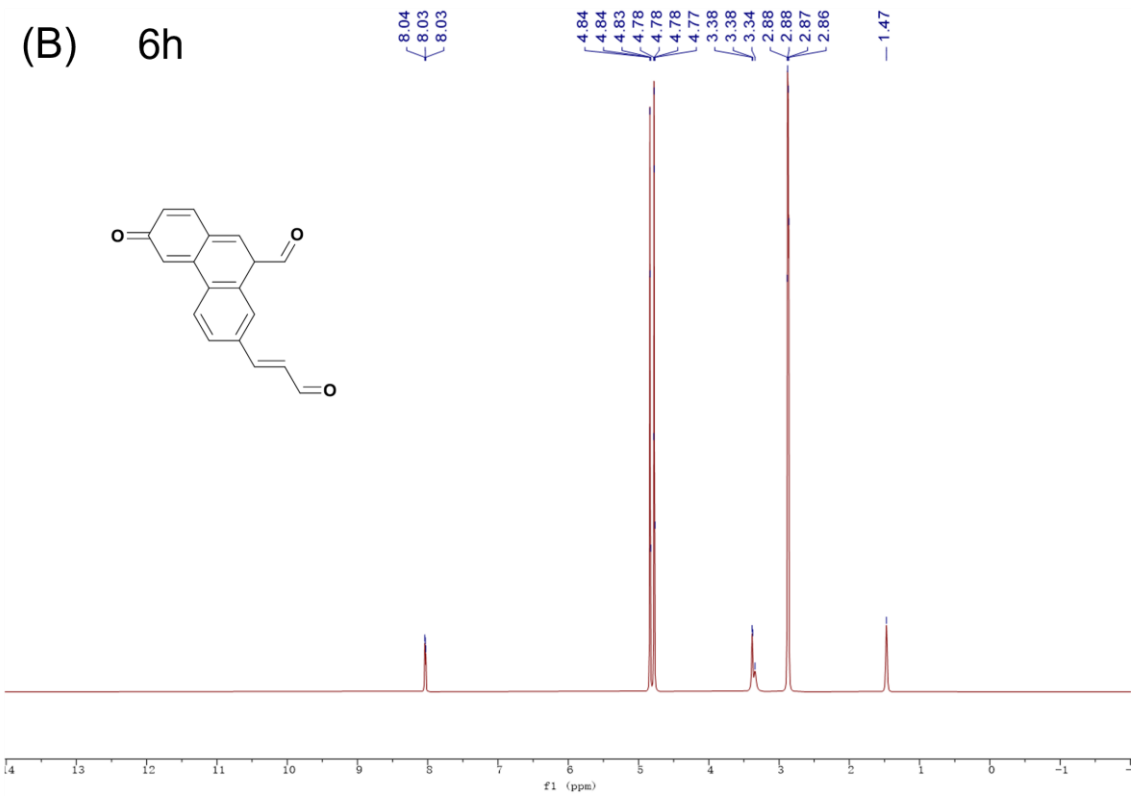

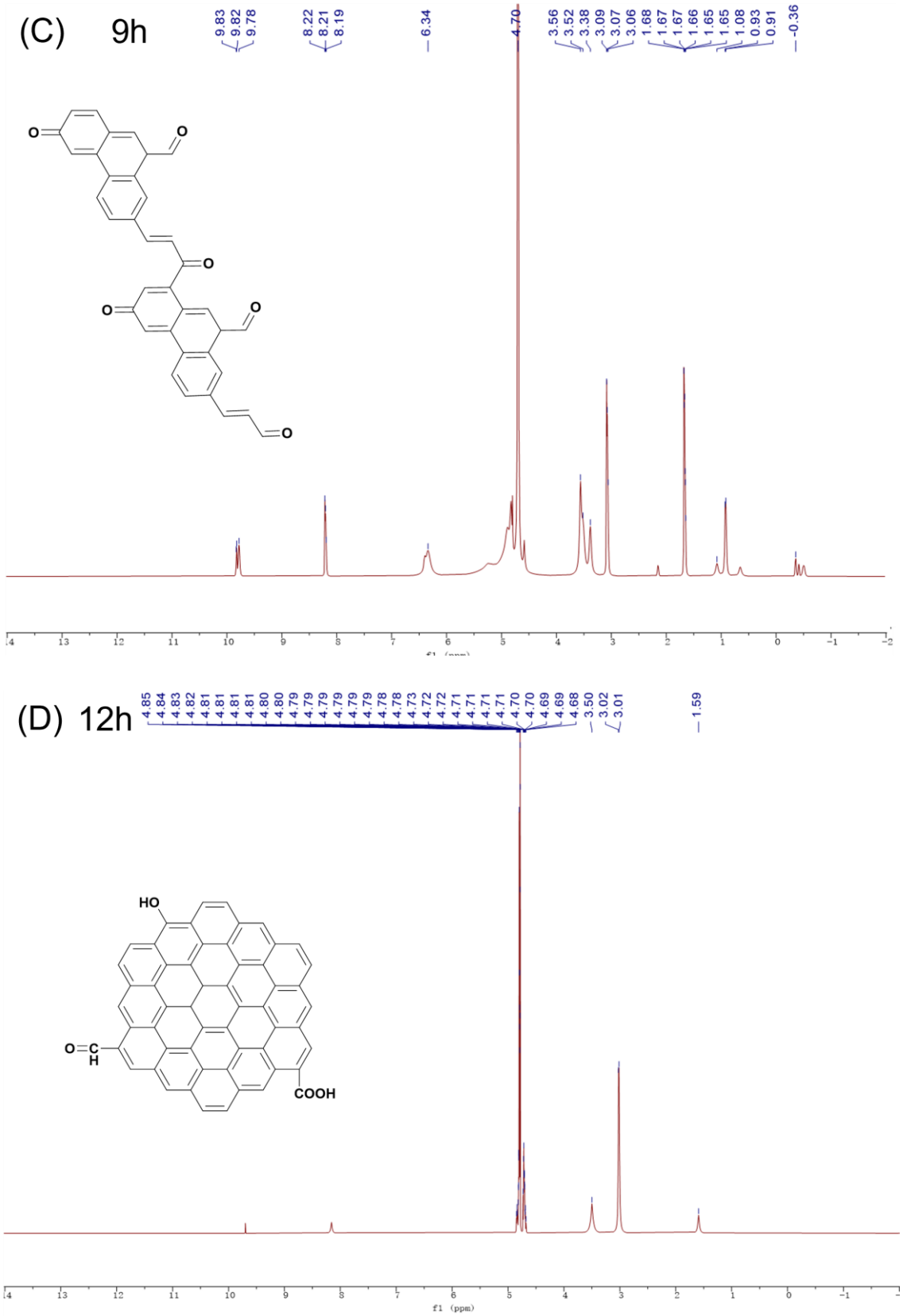

Figure S15. ^{1}HNMR spectrum (in D_2O) at reaction times of 3h (A), 6h (B), 9h (C), and 12h (D).

The formation mechanism involves a two-step process: First, the cleavage of lignin to produce aromatic compounds, and then the subsequent rearrangement and carbonization leading to the

formation of GQDs. Lignin, an amorphous polymer composed of phenylpropane units, is primarily interconnected through ether bonds or carbon-carbon bonds, with the β-O-4 ether bond being the predominant type, comprising approximately 60%-70% of the total bonds. In the first step, NaOH facilitates the cleavage of ether bonds in lignin, resulting in the generation of intermediate lignin fragments, alongside the formation of aromatic monomers bearing phenolic hydroxyl groups. These aromatic monomers serve as molecular precursors for GQD synthesis, leading to the formation of large polycyclic aromatic hydrocarbons through hydrothermal treatment. To gain further insights into the hydrothermal process and the formation mechanism, ^{1}H NMR spectroscopy was employed to study the evolution of the hydrochemical environment, as shown in **Figure S15**. The observed chemical shifts are attributed as follows:

δ = 1-2 ppm: C-H in methoxy group. The peak intensity and diversity increased between 3 and 9 hours, indicating the removal of methyl groups from the lignin structure, resulting in rising and broadening peaks. At 12 hours, the peaks exhibit a weak, narrow singlet state due to carbonization.

δ = 3-4 ppm: C-H in ether bond. The peak intensity reached its highest at 3 hours and lowest at 6-12 hours, indicating a significant cleavage of the ether bond during the reaction.

δ = 4-5 ppm: Aromatic hydrogen on polycyclic aromatic hydrocarbons (PAHs). No significant peak was observed within the first 3 hours. However, a substantial increase was observed at 6 hours, which stabilized at 12 hours. This rise is attributed to changes in the electronic environment within the conjugated regions, caused by the aggregation of aromatic monomers. The high singlets observed at 12 hours indicate a significant change in the chemical positions of hydrogen atoms within the fused aromatic ring.

δ = 6-8 ppm: H on monophenyl ring compounds.

δ = 8-9 ppm: Hydrogen on the phenolic hydroxyl group.

δ = 9-10 ppm: Carbonyl or carboxyl hydrogen.

Hydrogen peaks corresponding to different benzene rings in the lignin monomer appeared within 3 hours. Additionally, Y-GQDs exhibited significant peaks at 8-9 ppm, indicating the presence of hydroxyl groups. After 6 hours of reaction, the hydrogen signal intensity of each benzene ring decreased, while the concentration increased, providing evidence for the polymerization and dehydrogenation of aromatic compounds. Peaks between 9 and 10 ppm suggested the oxidation of hydroxyl groups into carbonyl and carboxyl groups. The peak intensity of benzene in the range of 6-8 ppm gradually decreased at 9 and 12 hours, ultimately reaching the minimum value. This reduction in hydrogen atoms attached to a single benzene

ring is attributed to dehydrogenation, leading to the formation of stable and extensive conjugated regions.

Importantly, the 3-hour spectra exhibited characteristic peaks corresponding to the monomers in the first step, confirming complete lignin cleavage. The 6-hour spectrum showed characteristic peaks associated with the end product of Step 2, while the 9-hour spectrum indicated further reactions of the aforementioned intermediates. Encouragingly, the 12-hour spectra demonstrated characteristic peaks corresponding to molten aromatics with intact conjugated regions. It is noteworthy that due to lignin's inherent heterogeneity, NMR spectroscopy captures different species rather than pure compounds. Consequently, the presence of characteristic peaks corresponding to intermediates at each time interval aids in evaluating the progress and extent of the reaction. In conclusion, the ^{1}H NMR analysis of Y-GQDs at different time points provides valuable insights into the reaction mechanism, confirming the initial decomposition of reactants into monomers followed by a vigorous polymerization and dehydrogenation reaction.

Supporting information 30: Illuminance diagram of individual UV chip.

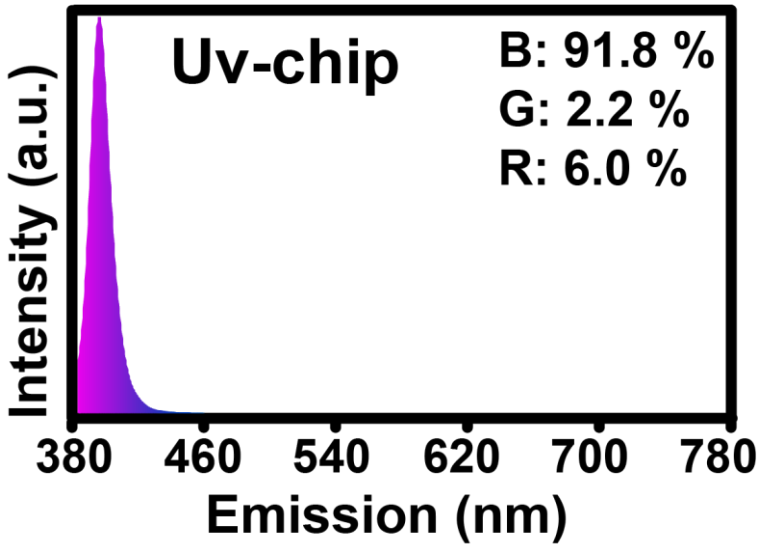

Figure S16. Illuminance diagram of purchased UV chip.

Supporting information 31: Stability demonstration of multi-colour LEDs.

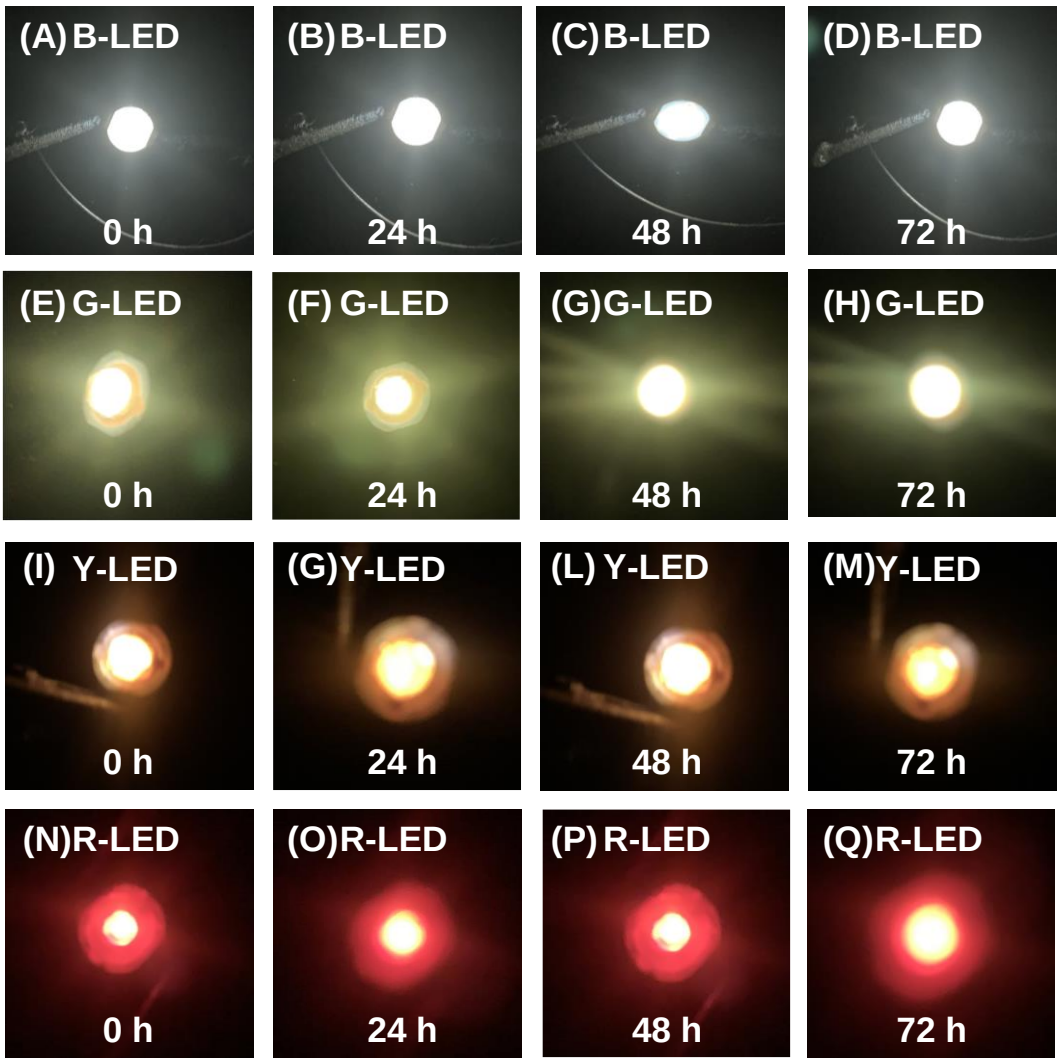

Figure S17. Photos illuminated by LEDs for 0 h, 24h, 48 h and 72 h.

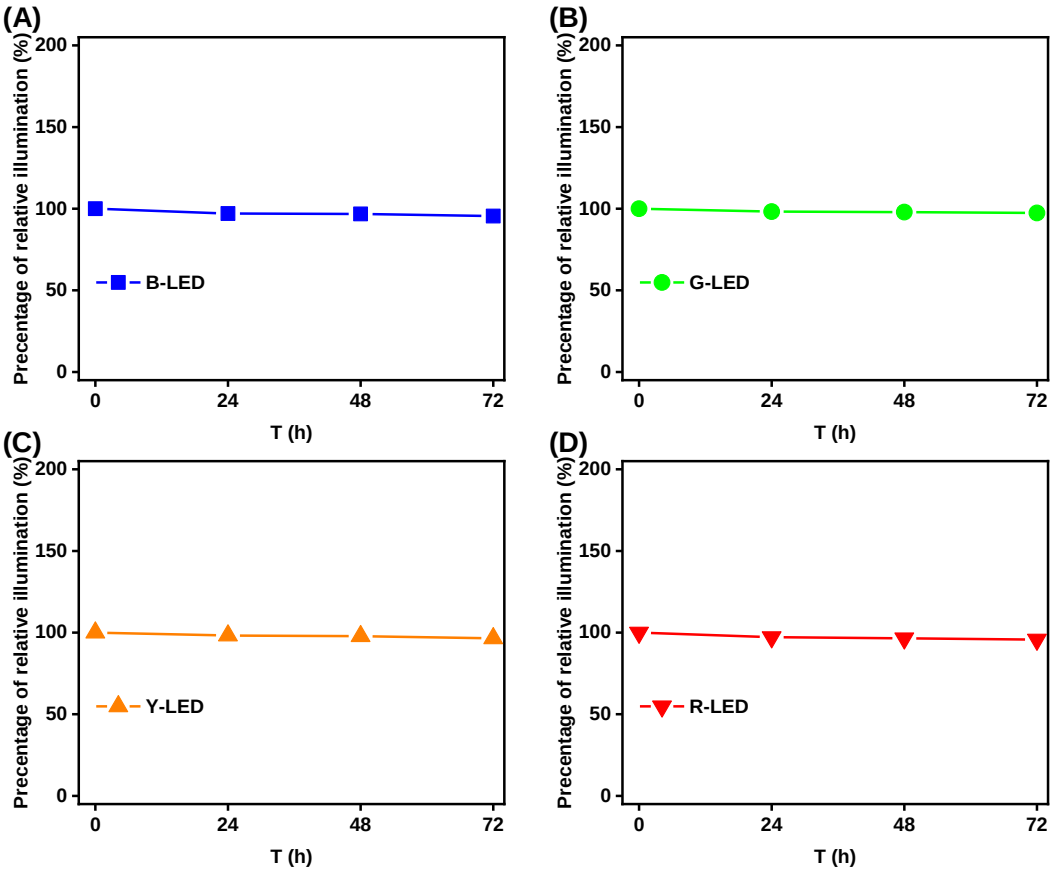

Figure S18. Percentage of relative illumination of LEDs irradiation 0 h, 24h, 48 h and 72 h.

Supporting information 32: Illumination of the UV lamp chip and four LEDs, along with the assessment of LED conversion efficiency.

Table S16. Illumination of UV lamp chip and four LEDs and LED conversion efficiency.

Sample	Illuminance (lx)	Emission Wavelength (nm)	LED conversion efficiency (%)
UV chip	40	410	/
B-LED	5.3	466	13.3
G-LED	4.5	579	11.3
Y-LED	2.8	651	7.1
R-LED	2.6	706	6.5

References

1. W. Chen, C. Hu, Y. Yang, J. Cui and Y. Liu, Materials, 2016, 9, 184.
2. S. Rai, B. K. Singh, P. Bhartiya, A. Singh, H. Kumar, P. K. Dutta and G. K. Mehrotra, J. Lumin., 2017, 190, 492-503.
3. Z. Ding, F. Li, J. Wen, X. Wang and R. Sun, Green Chem., 2018, 20, 1383-1390.
4. R. Wang, G. Xia, W. Zhong, L. Chen, L. Chen, Y. Wang, Y. Min and K. Li, Green Chem., 2019, 21, 3343-3352.
5. A. N. Nair, V. S. N. Chava, S. Bose, T. Zheng, S. Pilla and S. T. Sreenivasan, ACS Sustainable Chem. Eng., 2020, 8, 16565-16576.
6. J. Xu, P. Zhou, L. Dai, Y. Gui, L. Yuan, X. Shen, C. Zhang and K. Huo, Green Chem., 2021, 23, 6008-6019.
7. L. Zhu, D. Shen, Q. Liu, K. H. Luo and C. Li, ACS Sustainable Chem. Eng., 2022, 10, 9888-9898.
8. T. Zhang, J. Zhou, H. Li, J. Ma, X. Wang, H. Shi, M. Niu, Y. Liu, F. Zhang and Y. Guo, Green Chem., 2023, 25, 1406-1416.
9. T. F. Yeh, C. Y. Teng, S. J. Chen and H. Teng, Adv. Mater., 2014, 26, 3297-3303.